Compression-Designs of SAR Imagery Used as Prior Knowledge

Erlan H. Feria
The College of Staten Island (CSI) of the City University of New York (CUNY)
Department of Engineering Science and Physics
2800 Victory Blvd, Staten Island, New York, 10314
feria@mail.csi.cuny.edu

ABSTRACT

The signal to interference plus noise ratio (SINR) performance of SAR imagery knowledge-aided (KA) airborne moving target indicator (AMTI) radar subjected to severely taxing environmental disturbances is investigated for radar-blind and radar-seeing highly compressed SAR imagery. Radar-seeing schemes are found to greatly outperform radar-blind techniques.

Keywords: SAR imagery, radar-blind, radar-seeing, prior knowledge, compression-designs, source coding, knowledge-aided, intelligent system, intelligence processor, signal processing

1. INTRODUCTION

A real-world problem whose high performance is attributed to its use of an intelligent system (IS) is knowledge-aided (KA) airborne moving target indicator (AMTI) radar such as found in DARPA's knowledge aided sensory signal processing expert reasoning (KASSPER) [1]-[2]. The IS's intelligence, or prior knowledge, is clutter synthetic aperture radar (SAR) imagery and its intelligence processor (IP), or on-line computer, is the associated clutter covariance processor. Unfortunately, however, the excellent signal to interference plus noise ratio (SINR) radar performance achieved directly depends on satisfying prohibitively expensive storage and computational requirements. In this paper the former 'storage' problem is addressed using two general source coding approaches.

The area of source coding has a prominent recent history and has been one of the enabling technologies for what is known today as the information revolution. Examples of well established source coding schemes that have been offered in the past are lossless schemes such as Huffman Coding and Arithmetic Coding and lossy schemes such as JPEG, wavelets based JPEG2000, predictive-transform (PT) source coding, etc. [3]-[6]. In this paper two 'lossy' source-coding techniques are investigated for the inexpensive storage of SAR imagery. One of them is radar-blind since it is oblivious to the antenna pattern and range bin geometry (APRBG). It also uses PT source coding embedded in a novel simple and fast bit planes methodology which is shown in [6] to significantly outperform JPEG2000 in terms of 'local' signal to noise ratio (SNR) as well as 'global' SINR radar performance. An obvious advantage of a radar-blind approach is that it is universal due to its radar system independence. The second method is a radar-seeing one where the compression of the SAR image is achieved with knowledge of the APRBG. Of these two approaches only the radar-seeing one is found to yield outstanding SINR radar performance with high compression ratios. The SAR image used to obtain our results was that of the Mojave Airport in California which was compressed from 2MB to 512 bytes. For this compression ratio of 8,192 an average of average SINR error (AASE) of less than 1 dB for 64 range bins of the SAR image was derived.

In another paper [7] the simple and universal PT radar-blind technique is brought back to life when it is combined with an exceeding fast and novel intelligence processor that replaces the straight intelligence processor simulated in this paper.

This work was supported in part by the Defense Advanced Research Projects Agency (DARPA) under the KASSPER Program Grant No. FA8750-04-1-004.

Intelligent Computing: Theory and Applications IV, edited by Kevin L. Priddy, Emre Ertin,
Proc. of SPIE Vol. 6229, 62290J, (2006) · 0277-786X/06/$15 · doi: 10.1117/12.666403

The rest of this paper is organized as follows: In Section 2 the intelligent systems problem arising in KA-AMTI radar is stated. In Section 3 radar-blind and radar-seeing SAR compression schemes are advanced. Finally in Section 4 conclusions are drawn.

2. THE KA-AMTI RADAR PROBLEM

In Fig. 1 an overview of a radar system is shown. It consists of two major structures. These are: 1) An iso-range ring, or range bin, for a uniform linear array (ULA) in uniform constant-velocity motion relative to the ground: only the front of the iso-range ring is shown corresponding to angle displacements from -90^o to 90^o relative to the antenna array boresight; and 2) An AMTI radar composed of an antenna, a space-time processor (STP) and a detection device. In KA-AMTI clutter returns are available in the form of SAR imagery that is obtained from a prior viewing of the area of interest. From this figure it is also noticed that the range bin is decomposed into N_C clutter cells. N_C is often assumed to be greater than or equal to the degrees of freedom of the system NM [8]-[9] where N is the number of antenna elements and M is the number of transmitted antenna pulses during a coherent pulse interval (CPI). In the simulations it will be assumed N=16, M=16 and $N_C = 256$, see Table 1a-b which is located close to the end of the paper.

The general architecture of the STP is shown in Fig. 2. From this system it is first noted that its input consists of the addition of two signals. They are: 1) the signal **s** representing the steering vector of the target; 2) the signal **x** representing all system disturbances, which include the incident clutter, jammer, channel mismatch (CM), internal clutter motion (ICM), range walk (RW), antenna array misalignment (AAM), and thermal white noise (WN). Both of these signals are NM dimensional and complex and their space-time geometrical associations can be readily seen from Fig. 3. The salient characteristics of the signals and systems shown if Fig. 2 is next described in some detail. The discussion is structured as follows: first, the definition of the target steering vector s is given; second, the SINR radar performance criterion that is linked to the overall STP structure of Fig. 2 is stated; third the total disturbance covariance matrix appearing on the SINR criterion is defined using the covariance matrix tapers (CMTs) methodology of [9]; and fourth, the optimum direct inverse (DI) solution to the SINR criterion is given and the sample matrix inverse (SMI) is advanced as the not KA algorithm to use when determining the prerequisite disturbance covariance matrix. The section ends with SMI simulation results that motivate the need for KA algorithms.

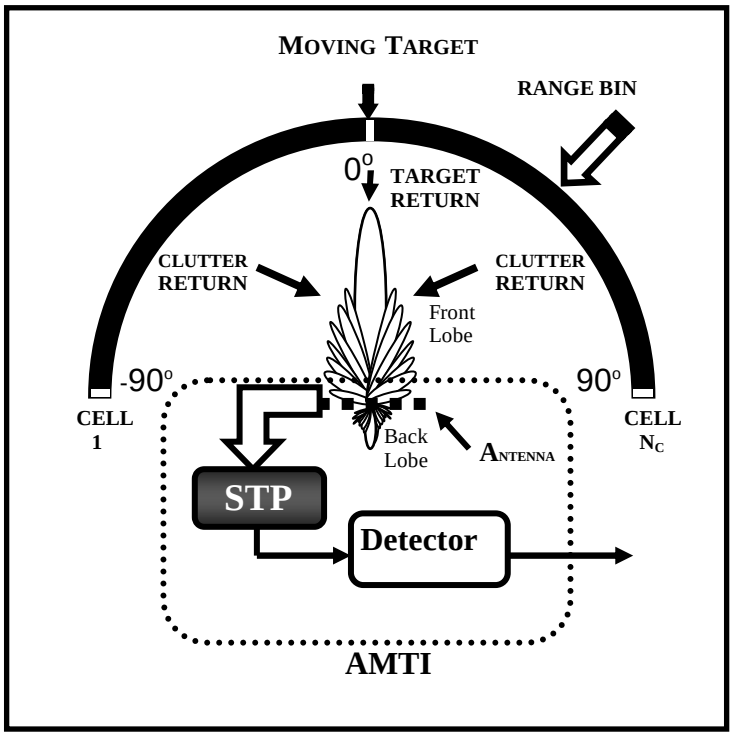

Fig. 1 The Overall Radar System

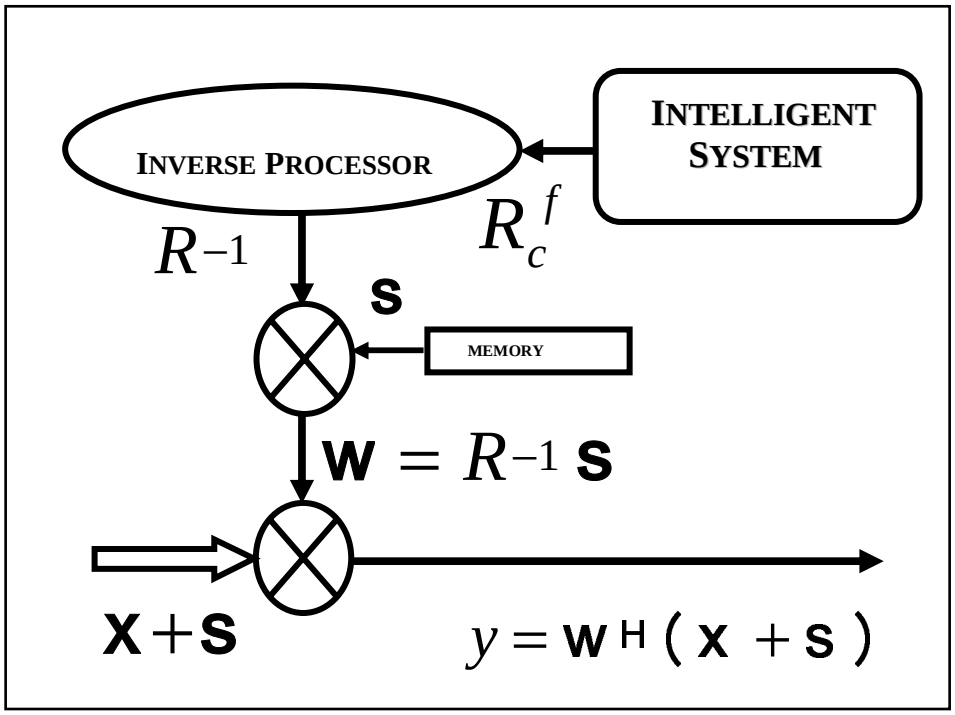

Fig. 2 The Space-Time Processor (STP)

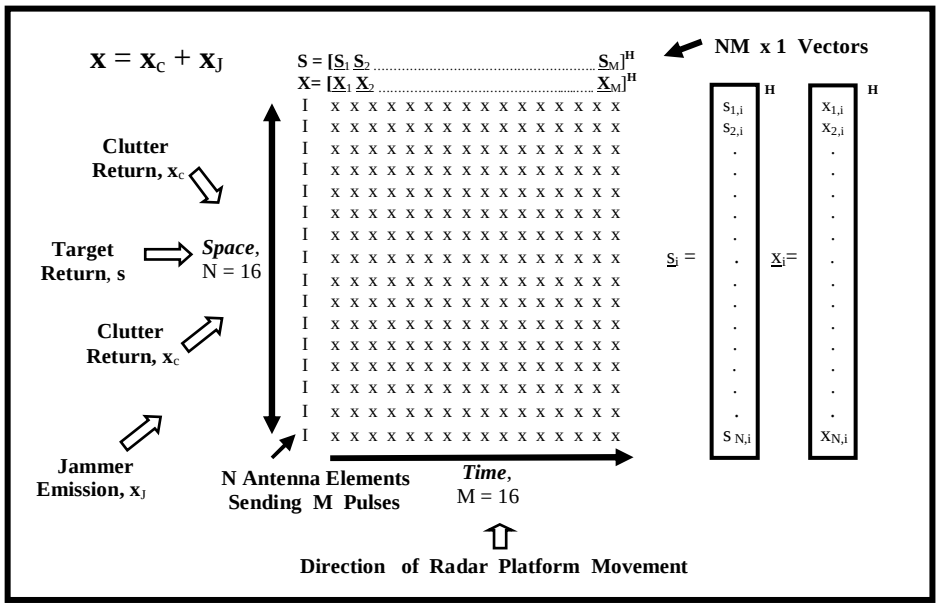

Fig. 3 Space-Time Signals Geometry

2.1. Target Steering Vector

In particular the target steering vector **s** is defined by the following relations [8]-[9]

$$\mathbf{s} = [\underline{\mathbf{s}}_1(\theta_t)\ \underline{\mathbf{s}}_2(\theta_t) \ldots . \underline{\mathbf{s}}_M(\theta_t)]^H \tag{2.1}$$

$$\underline{\mathbf{s}}_k(\theta_t) = e^{j2\pi(k-1)\overline{f}_D^t}\,\underline{\mathbf{s}}_1(\theta_t) \quad for\ k = 1,\ldots,M \tag{2.2}$$

$$\underline{s}_1(\theta_t) = [s_{1,1}(\theta_t)\ \ s_{2,1}(\theta_t)\ \ ....\ \ s_{N,1}(\theta_t)] \tag{2.3}$$

$$s_{k,1}(\theta_t) = e^{j2\pi(k-1)\bar{\theta}_t} \quad for\ k = 1,\ldots,N \tag{2.4}$$

$$\bar{f}^{\,t}_D = f^t_D / f_r \tag{2.5}$$

$$f^t_D = 2v_t / \lambda \tag{2.6}$$

$$f_r = 1/T_r \tag{2.7}$$

$$\bar{\theta}_t = \frac{d}{\lambda}\sin(\theta_t) \tag{2.8}$$

where: a) θ_t is the angle of attack (AoA) of the target with respect to boresight (in the simulations this angle is 0^o, see Table 1c); b) d is the antenna inter-element spacing; c) λ is the operating wavelength (in the simulations $d/\lambda = ½$, see Table 1a); d) $\bar{\theta}_t$ is the normalized θ_t; e) T_r is the pulse repetition interval (PRI); f) f_r is the pulse repetition frequency (PRF) (in the simulations $f_r = 10^3$ Hz, see Table 1a); g) v_t is the target radial velocity; h) f^t_D is the Doppler of the target; and i) $\bar{f}^{\,t}_D$ is the normalized f^t_D.

2.2. Radar Performance Criterion

The input of the STP, **x**+**s,** is multiplied by the complex transposition of a NM x 1 dimensional weight vector **w** to yield a scalar but complex output $y = \mathbf{w}^H(\mathbf{x}+\mathbf{s})$. The assigned task to the weight vector **w** is to produce a ratio of the power of the signal term $\mathbf{w}^H\mathbf{s}$, i.e., $\mathbf{w}^H\mathbf{s}\mathbf{s}^H\mathbf{w}$, to the power of the disturbance term $\mathbf{w}^H\mathbf{x}$, i.e., $\mathbf{w}^H\mathrm{R}\mathbf{w}$ where $\mathrm{R}=\mathrm{E}[\mathbf{x}\mathbf{x}^H]$, that is as large as possible. This so-called signal to interference plus noise ratio (SINR) is a simple and natural measure of radar performance and is written in the following manner

$$\mathrm{SINR} = \mathbf{w}^H\mathbf{s}\mathbf{s}^H\mathbf{w} / \mathbf{w}^H\mathrm{R}\mathbf{w} \tag{2.9}$$

2.3. Total Disturbance Covariance

The NM x NM dimensional matrix, R, denotes the total disturbance covariance. To model this covariance the covariance matrix tapers (CMTs) formulation of [9] is used which is as follows:

$$\mathrm{R} = \{\mathrm{R_C}\ \ \mathrm{O}\ \ (\mathrm{R_{RW}} + \mathrm{R_{ICM}} + \mathrm{R_{CM}})\} + \{\mathrm{R_J}\ \ \mathrm{O}\ \ \mathrm{R_{CM}}\} + \mathrm{R_n} \tag{2.10}$$

$$R_C = R_c^f + R_c^b \tag{2.11}$$

where $\mathrm{R_n}$, R_c^f, R_c^b, $\mathrm{R_C}$, $\mathrm{R_J}$, $\mathrm{R_{RW}}$, $\mathrm{R_{ICM}}$ and $\mathrm{R_{CM}}$ are covariance matrices of dimension NM x NM and the symbol O denotes a Hadamard product or element by element multiplication. Moreover these disturbance covariances correspond to: $\mathrm{R_n}$ to thermal white noise; R_c^f to front clutter; R_c^b to back clutter; $\mathrm{R_C}$ to total clutter; $\mathrm{R_J}$ to jammer; $\mathrm{R_{RW}}$ to range walk; $\mathrm{R_{ICM}}$ to internal clutter motion ; and $\mathrm{R_{CM}}$ to channel mismatch. In [9] the covariances $\mathrm{R_{RW}}$, $\mathrm{R_{ICM}}$ and $\mathrm{R_{CM}}$ are referred as CMTs. The composite covariances in (2.10)-(2.11) are now defined in detail.

2.3.1. Thermal White Noise

The thermal white noise covariance R_n is defined as

$$R_n = \sigma_n^2 I_{NM} \tag{2.12}$$

where σ_n^2 is the average power of thermal white noise (assumed one in our simulations, see Table 1d) and $\mathrm{I_{NM}}$ is an identity matrix of dimension NM by NM.

2.3.2. Front Clutter

The front clutter covariance R_c^f is defined as

$$R_c^f = \sum_{i=1}^{N_C} p_c^f(\theta_c^i, \theta_t)\mathrm{c}^f(\theta_c^i, \theta_{AAM})\mathrm{c}^f(\theta_c^i, \theta_{AAM})^H \tag{2.13}$$

$$p_{c}^{f}(\theta_c^i,\theta_t) = G_{A}^{f}(\theta_c^i,\theta_t)\ {}_f\sigma_{c,i}^2 \tag{2.14}$$

$$G_{A}^{f}(\theta_c^i,\theta_t) = K^f \left|\sin\left\{N\pi\frac{d}{\lambda}(\sin(\theta_c^i)-\sin(\theta_t))\right\}/\sin\left\{\pi\frac{d}{\lambda}(\sin(\theta_c^i)-\sin(\theta_t))\right\}\right|^2 \tag{2.15}$$

$$\mathrm{c}^{f}(\theta_c^i,\theta_{AAM}) = [{}_f\underline{\mathrm{c}}_1(\theta_c^i,\theta_{AAM})\ \ {}_f\underline{\mathrm{c}}_2(\theta_c^i,\theta_{AAM})\cdots{}_f\underline{\mathrm{c}}_M(\theta_c^i,\theta_{AAM})]^H \tag{2.16}$$

$${}_f\underline{\mathbf{c}}_k(\theta_c^i,\theta_{AAM}) = e^{j2\pi(k-1)\bar{f}_D^{c_f}(\theta_c^i,\theta_{AAM})}\underline{\mathbf{c}}_1(\theta_c^i) \tag{2.17}$$

$$for\ k = 1,\ldots, M$$

$$\underline{\mathrm{c}}_1(\theta_c^i) = [\mathrm{c}_{1,1}(\theta_c^i)\ \ \mathrm{c}_{2,1}(\theta_c^i)\ \ \ldots.\ \mathrm{c}_{N,1}(\theta_c^i)] \tag{2.18}$$

$$\mathrm{c}_{k,1}(\theta_c^i) = e^{j2\pi(k-1)\bar{\theta}_c^i}\quad for\ k = 1,\ldots, N \tag{2.19}$$

$$\bar{f}_{D}^{c_f}(\theta_c^i,\theta_{AAM}) = \beta\bar{\theta}_C^i\{\cos(\theta_{AAM}) + \sqrt{\sin^2(\theta_{AAM}) + (\cos^2(\theta_{AAM})-1)\sin^2(\theta_C^i)}\,/\sin(\theta_C^i)\} \tag{2.20}$$

$$\beta = (v_p T_r)/(d/2) \tag{2.21}$$

$$\bar{\theta}_c^i = (d/\lambda)\sin(\theta_c^i) \tag{2.22}$$

where: a) the index i refers to the i-th front clutter cell on the range bin section shown on Fig. 1; b) θ_c^i is the AoA of the i-th clutter cell; c) θ_{AAM} is the antenna array misalignment angle (assumed 2° in our simulations, see Table 1d) [8]-[9]; d) ${}_f\sigma_{c,i}^2$ is the i-th front clutter source cell power (excluding the antenna gain); e) $G_{A}^{f}(\theta_c^i,\theta_t)$ is the antenna pattern gain associated with the i-th front clutter cell; f) K^f is the front global antenna gain (assumed $4\text{x}10^5$ or 56 dBs in our simulations, see Table 1a); g) $p_{C}^{f}(\theta_c^i,\theta_t)$ is the "total" i-th front clutter cell power (in the simulations the 4 MBs SAR image of the Mojave Airport in California of Fig. 4 is used [2] where: i) this figure depicts the resolution clutter source cell power in dBs; ii) the down range is 1500 meters represented by 1024 rows; and iii) the cross range is 1800 meters represented by 256 columns. In addition, groups of sixteen consecutive rows are averaged to yield the 64 range bins depicted in Fig. 5 and Fig. 6 presents the front clutter to noise ratio (CNR^{f}), i.e.,

$$CNR^f = R_c^f(1,1)/\sigma_n^2 = \sum_{i=1}^{N_C} p_c^f(\theta_c^i,\theta_t)/\sigma_n^2, \tag{2.23}$$

for the 64 range bins with values ranging from 41 to 75 dBs as noted in Table 1b); h) $c^f(\theta_c^i,\theta_{AAM})$ is the NM x 1

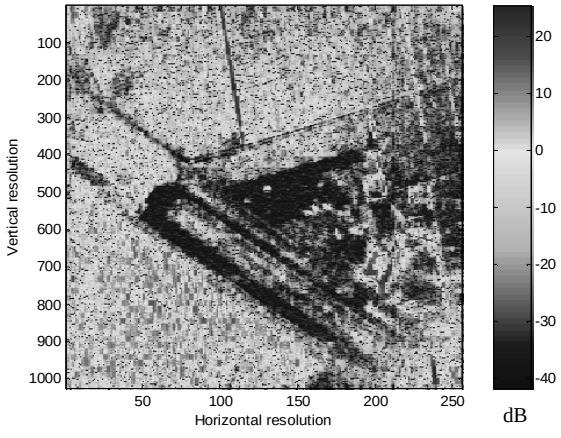

Fig. 4 1024 x 256 4MB SAR Image

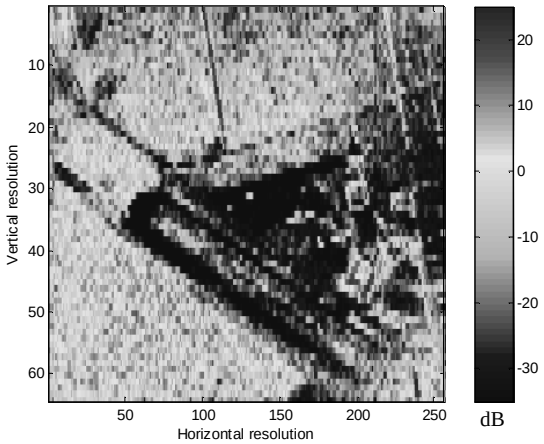

Fig. 5 64 Range Bins of SAR Image

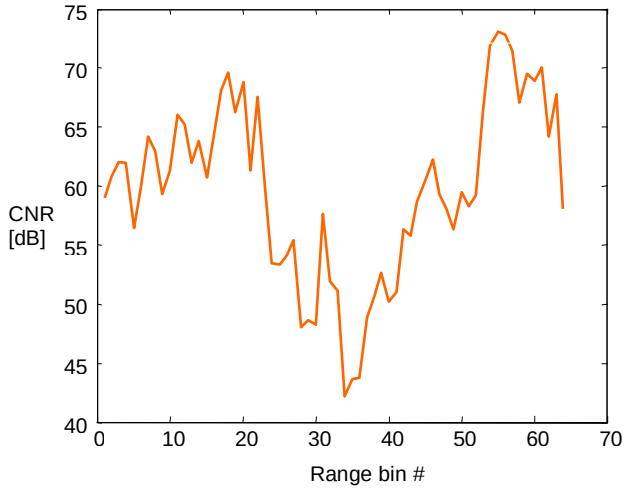

Fig. 6 CNR vs Range Bin #

dimensional and complex i-th clutter cell steering vector; i) v_p is the radar platform speed; j) $\bar{\theta}_c^i$ is the normalized θ_c^i; and k) β is the ratio of the distance traversed by the radar platform during the PRI, $v_p T_r$, to the half antenna inter-element distance, d/2 (β is assumed to be one in our simulations, see Table 1b).

2.3.3. Back Clutter

The back clutter covariance R_c^b is given by

$$R_c^b = \sum_{i=1}^{N_C} p_c^b(\theta_c^i, \theta_t) \mathrm{c}^b(\theta_c^i, \theta_{AAM}) \mathrm{c}^b(\theta_c^i, \theta_{AAM})^H \quad (2.24)$$

$$p_C^b(\theta_c^i, \theta_t) = G_A^b(\theta_c^i, \theta_t)\, {}_b\sigma_{c,i}^2 \quad (2.25)$$

$$G_A^b(\theta_c^i, \theta_t) = K^b \left| \sin\left\{ N\pi \frac{d}{\lambda}(\sin(\theta_c^i) - \sin(\theta_t)) \right\} / \sin\left\{ \pi \frac{d}{\lambda}(\sin(\theta_c^i) - \sin(\theta_t)) \right\} \right|^2 \quad (2.26)$$

$$\mathrm{c}^b(\theta_c^i, \theta_{AAM}) = [{}_b\underline{c}_1(\theta_c^i, \theta_{AAM})\ \ {}_b\underline{c}_2(\theta_c^i, \theta_{AAM}) \ldots {}_b\underline{c}_M(\theta_c^i, \theta_{AAM})]^H \quad (2.27)$$

$${}_b\underline{c}_k(\theta_c^i, \theta_{AAM}) = e^{j2\pi(k-1)\bar{f}_D^{c_b}(\theta_c^i, \theta_{AAM})}\, \underline{c}_1(\theta_c^i) \quad (2.28)$$

$$for\ k = 1, \ldots, M$$

$$\bar{f}_D^{c_b}(\theta_c^i, \theta_{AAM}) = \beta\bar{\theta}_c^i \{\cos(\theta_{AAM}) - \sqrt{\sin^2(\theta_{AAM}) + (\cos^2(\theta_{AAM}) - 1)\sin^2(\theta_c^i)}\,/\sin(\theta_c^i)\} \quad (2.29)$$

where: a) the index i now refers to the i-th clutter cell on the back side of the iso-range ring, not shown in Fig. 1; b) θ_c^i is the AoA of the i-th back clutter cell; c) ${}_b\sigma_{c,i}^2$ is the i-th back clutter source cell power (assumed one for all i in our simulations, see Table 1b); d) $G_A^b(\theta_c^i, \theta_t)$ is the back antenna pattern gain associated with ${}_b\sigma_{c,i}^2$; e) K^b is the global back antenna gain (assumed 10^{-4} in our simulations, see Table 1a); f) $p_C^b(\theta_c^i, \theta_t)$ is the total clutter cell power of the i-th back clutter cell (in our simulations the back clutter to noise ratio, CNR^b, defined by

$$CNR^b = R_c^b(1,1)/\sigma_n^2 = \sum_{i=1}^{N_C} p_c^b(\theta_c^i, \theta_t)/\sigma_n^2, \quad (2.30)$$

is assumed to be -40 dBs, see Table 1b); f) $\mathrm{c}^b(\theta_c^i, \theta_{AAM})$ is the NM x 1 dimensional and complex steering vector associated with ${}_b\sigma_{c,i}^2$; and g) $\underline{c}_1(\theta_c^i)$ is as defined in (2.18)-(2.19).

2.3.4. Jammer

The jammers covariance R_J is given by

$$R_J = \sum_{i=1}^{N_J} p_J(\theta_J^i, \theta_t)(I_M \otimes 1_{N\times N})\, \mathrm{O}(\mathrm{j}(\theta_J^i) \bullet \mathrm{j}(\theta_J^i)^H) \quad (2.31)$$

$$p_J(\theta_J^i, \theta_t) = G_A^f(\theta_J^i, \theta_t)\, \sigma_{J,i}^2 \quad (2.32)$$

$$\mathrm{j}(\theta_J^i) = [\mathbf{j}_1(\theta_J^i)\ \ \mathbf{j}_2(\theta_J^i) \ldots . \mathbf{j}_M(\theta_J^i)]^H \quad (2.33)$$

$$\mathbf{j}_k(\theta_J^i) = \mathbf{j}_1(\theta_J^i) \quad for\ k = 1, \ldots, M \quad (2.34)$$

$$\mathbf{j}_1(\theta_J^i) = [\mathrm{j}_{1,1}(\theta_J^i)\ \ \mathrm{j}_{2,1}(\theta_J^i)\ \ ....\ \ \mathrm{j}_{N,1}(\theta_J^i)] \tag{2.35}$$

$$j_{k,1}(\theta_J^i) = e^{j2\pi(k-1)\bar{\theta}_J^i} \quad for\ k = 1,...,N \tag{2.36}$$

$$\bar{\theta}_J^i = \frac{d}{\lambda}\sin(\theta_J^i) \tag{2.37}$$

where: a) the index i refers to the i-th jammer on the range bin; b) N_J is the total number of jammers (assumed three in our simulations, see Table 1e) ; c) θ_J^i is the AoA of the i-th jammer (the location of the three assumed jammers are at -60°, -30°, and 45° in our simulations, see Table 1e); d) $\otimes$ is the Kronecker (or tensor) product [8]; e) I_M is an identity matrix of dimension M by M; f) 1_{NxN} is a unity matrix of dimension N by N; g) $\sigma_{J_i}^2$ is the i-th jammer power (in the simulations 34 dBs is assumed for the three jammers considered, see Table 1e); h) $p_J(\theta_c^i, \theta_t)$ is the "total" i-th jammer power (in our simulations the jammer to noise ratio (JNR), defined by

$$JNR = R_J(1,1)/\sigma_n^2 = \sum_{i=1}^{N_J} p_J(\theta_c^i, \theta_t)/\sigma_n^2, \tag{2.38}$$

is given by 53, -224, and 66 dBs for the jammers at -60°, -30°, and 45°, respectively, see Table 1e); and i) $\mathbf{j}(\theta_J^i)$ is the NM x 1 dimensional and complex i-th jammer steering vector that is noted from the defining equations (2.33)-(2.37) to be Doppler independent.

2.3.5. Range walk

The range walk or RW CMT, R_{RW} , is given by

$$R_{RW} = R_{RW}^{time} \otimes R_{RW}^{space} \tag{2.39}$$

$$[R_{RW}^{time}]_{i,k} = \rho^{|i-k|} \tag{2.40}$$

$$R_{RW}^{space} = 1_{NxN} \tag{2.41}$$

$$\rho = \Delta A / A = \Delta A / \{\Delta R \Delta\theta\} = \Delta A / \{(c/B)\Delta\theta\} \tag{2.42}$$

where: a) c is the velocity of light; b) B is the bandwidth of the compressed pulse; c) ΔR is the range-bin radial width; d) Δθ is the mainbeam width; e) A is the area of coverage on the range bin associated with Δθ at the beginning of the range walk; f) ΔA is the remnants of area A after the range bin migrates during a CPI; and g) ρ is the fractional part of A that remains after the range walk (in the simulations ρ=0.999999, see Table 1f) .

2.3.6. Internal Clutter Motion

The internal clutter motion or ICM CMT [9], R_{ICM} , is given by

$$R_{ICM} = R_{ICM}^{time} \otimes R_{ICM}^{space} \tag{2.43}$$

$$[R_{ICM}^{time}]_{i,k} = \frac{r}{r+1} + \frac{1}{r+1}\frac{(bc)^2}{(bc)^2 + (4\pi f_c |k-i| T_r)^2} \tag{2.44}$$

$$R_{ICM}^{space} = 1_{NxN} \tag{2.45}$$

$$10\log_{10} r = -15.5\log_{10}\omega - 12.1\log_{10} f_c + 63.2 \tag{2.46}$$

where: a) f_c is the carrier frequency in megahertz; b) ω is the wind speed in miles per hour; c) r is the ratio between the dc and ac terms of the clutter Doppler power spectral density; d) b is a shape factor that has been tabulated; and e) c is the speed of light. In the simulations f_c = 1,000 MHz, ω = 15 mph and b = 5.7, see Table 1a,g.

2.3.7. Channel Mismatch

The total channel mismatch or CM CMT, R_{CM} , is given by

$$R_{CM} = R_{NB} \text{ O } R_{FB} \text{ O } R_{AD} \tag{2.47}$$

where R_{NB}, R_{FB} and R_{AD} are composite CMTs [9] that are defined next:

2.3.7.1. Angle Independent Narrowband

R_{NB} is an angle-independent narrowband or NB channel mismatch CMT [9] given by

$$R_{NB} = \mathbf{q}\mathbf{q}^H \tag{2.48}$$

$$\mathbf{q} = \left[\underline{q}_1 \ \underline{q}_2 \ldots \underline{q}_M\right]^H \tag{2.49}$$

$$\underline{q}_k = \underline{q}_1 \quad for\ k = 1,..,M \tag{2.50}$$

$$\underline{q}_1 = \left[\varepsilon_1 e^{j\gamma_1} \ \varepsilon_2 e^{j\gamma_2} \ \ldots \ \varepsilon_N e^{j\gamma_N}\right] \tag{2.51}$$

where in (2.51) $\Delta\varepsilon_1,\ldots,\Delta\varepsilon_N$ and $\Delta\gamma_1,\ldots,\Delta\gamma_N$ denote amplitude and phase errors, respectively. In the simulations the amplitude errors are assumed to be zero and the phase errors to fluctuate with a 5^o root mean square (rms), see Table 1h.

2.3.7.2. Finite Bandwidth

R_{FB} is a finite (nonzero) bandwidth or FB channel mismatch CMT [9] given by

$$R_{FB} = R_{FB}^{time} \otimes R_{FB}^{space} \tag{2.52}$$

$$R_{FB}^{time} = 1_{MxM} \tag{2.53}$$

$$[R_{FB}^{space}]_{i,k} = (1-\Delta\varepsilon/2)^2 \sin c^2(\Delta\phi/2) \quad for \quad i \neq k \tag{2.54}$$

$$[R_{FB}^{space}]_{i,i} = 1-\Delta\varepsilon+\frac{1}{3}\Delta\varepsilon^2 \quad for \quad i = 1,..,N \tag{2.55}$$

where in (2.54)-(2.55) $\Delta\varepsilon$ and $\Delta\phi$ denote the peak deviations of decorrelating random amplitude and phase channel mismatch, respectively (note that the square term in (2.55), i.e., $\Delta\varepsilon^2$, corrects an error in [9] where it is shown as $\Delta\varepsilon^3$). In the simulations $\Delta\varepsilon$ = 0.001 and $\Delta\phi$ = 0.1 ^{o}, see Table 1i (notice that these values in conjunction with the correct equations (2.54)-(2.55) yield approximately the same results as those reported in [9] when the aforementioned incorrect equations were simulated with $\Delta\varepsilon$ = 0.01 and $\Delta\phi$ = 1).

2.3.7.3. Angle Dependent

R_{AD} is a reasonably approximate angle-independent CMT for angle-dependent or AD channel mismatch [9] given by

$$R_{AD} = R_{AD}^{time} \otimes R_{AD}^{space} \tag{2.56}$$

$$R_{AD}^{time} = 1_{MxM} \tag{2.57}$$

$$[R_{AD}^{space}]_{i,k} = \text{sinc}(B|k-i|\frac{d}{c}\sin(\Delta\theta)) \ for \ \ i \neq k \tag{2.58}$$

$$[R_{AD}^{space}]_{i,i} = 1 \tag{2.59}$$

where B is the bandwidth of an ideal bandpass filter and $\Delta\theta$ is a suitable measure of mainbeam width. In the simulations B = 100 MHz and $\Delta\theta$ = 28.6^o, see Table 1j.

2.4. Optimum Direct Inverse

The **w** that maximizes the SINR expression (2.9) is given by the following expression [8]-[9]

$$\mathbf{w} = \mathrm{R}^{-1}\mathbf{s}. \tag{2.60}$$

Two general approaches can be used to derive R. They are:

1) The first approach is not knowledge-aided and is given by the SMI expression [8]-[9]

$$^{smi}R = \frac{1}{Lsmi}\sum_{i=1}^{Lsmi} X_i X_i^H + \sigma^2_{diag} I \tag{2.61}$$

where X_i denotes radar measurements from range bins close to the range bin under investigation, Lsmi is the number of measurement samples and σ^2_{diag}I is a diagonal loading term. When performing our investigations X_i was derived via the following generating expression

$$X_i = R_i^{-1/2}\mathbf{x}_i \tag{2.62}$$

where: a) $\mathbf{x}_i$ is a zero mean, unity variance, NM dimensional complex random draw; and b) R_i is the total disturbance covariance (2.10)-(2.11) associated with the i-th range bin. In the simulations $\sigma^2_{diag} = 10\sigma^2_n$ =10 [9], see Table 1k.

2) The second approach is KA and assumes knowledge of all the covariances associated with the total disturbance covariance R, see (2.10)-(2.11).

2.6. Sample Matrix Inverse Simulation Results

In Figs. 7 and 8 the first simulation results are presented. They pertain to the use of the optimum direct inverse scheme (2.60) in conjunction with the SMI algorithm (2.61)-(2.62) to yield

$$\mathbf{w} = [^{smi}R]^{-1}\mathbf{s}. \tag{2.63}$$

where Lsmi = 512. This integer of Lsmi corresponds to having the 64 range bins of Fig. 5 scanned eight times. These results were also obtained using the simulation parameters summarized in Table 1. It should be emphasized that these

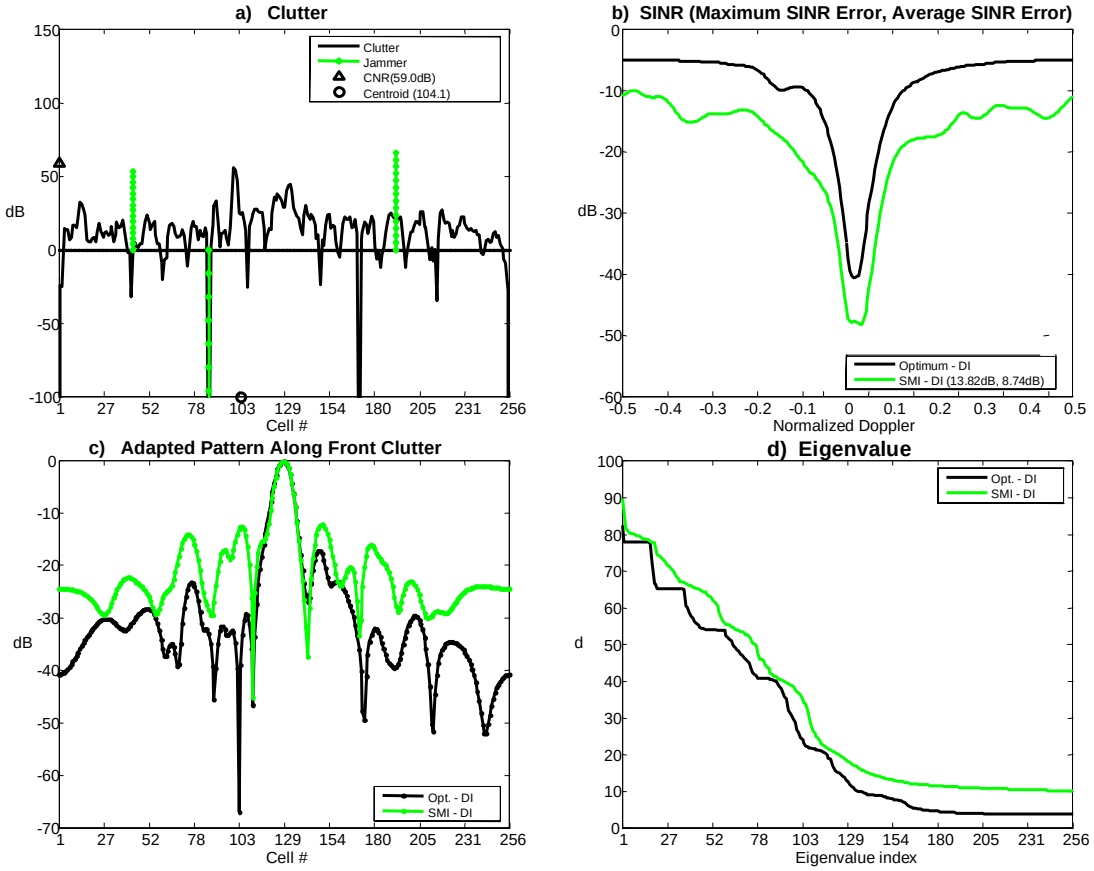

Fig. 7 SMI Simulation Results for Lsmi = 512 and Range Bin #1

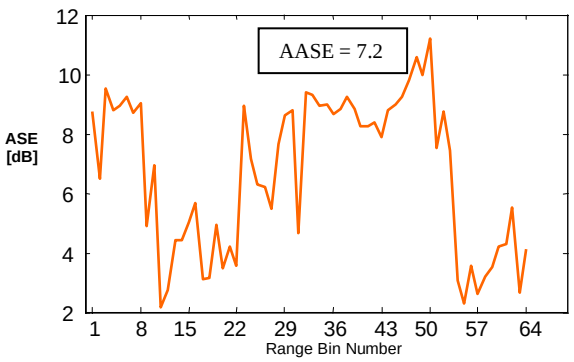

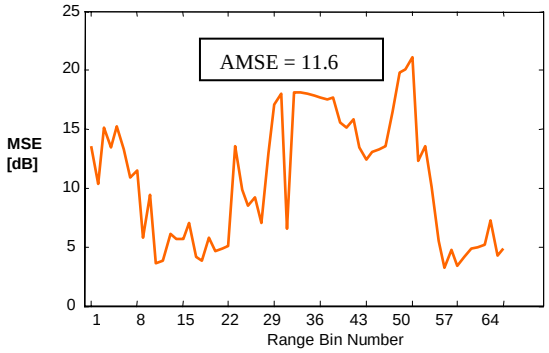

Fig. 8 a) SMI Average SINR Error (ASE) versus Range Bin b) SMI Maximum SINR Error (MSE) versus Range Bin Number

values are typical real-world radar system parameters that were used in [9] to illustrate some of the STAP techniques discussed there. The results presented in Figs. 7 and 8 are now discussed since they motivate the study of the KA techniques of Section 3.

Fig. 7 pertains to range bin # 1 of Fig. 5. This range bin cuts across a high elevation airport fence which is located on the upper half of the SAR image. From Fig. 7a it is first noted how the front clutter average power $p_C^f(\theta_c^i, \theta_t)$ varies in dBs with respect to range bin cell position (note from Fig. 1 that range bin cell position 1 corresponds to -90°, 128.5 to 0° and 256 to +90°, all angles measured from boresight). Furthermore, on the average power axis the corresponding CNR value of 59 dB is marked and on the cell position axis the range bin centroid (see [7] for its definition) value of 104.1 which is noted to reside 24.4 range bin cells away (-17.1°) from the assumed target location of 128.5 or 0°. In Fig. 7b the optimum and SMI SINR plots are displayed versus normalized Doppler. In particular, for the SMI SINR plot the average SINR error of 8.74 dBs and the maximum SINR error of 13.82 dBs are noted. In Fig. 7c the SMI adapted pattern is given in dBs along the front clutter ridge which is defined as follows

$$AP(\theta_c^i, \theta_{AAM}, \beta, \theta_t, f_D^t) = 10\log_{10}\left|\mathbf{w}^H \mathbf{c}^f(\theta_c^i, \theta_{AAM})\right|^2 \tag{2.64}$$

where $\theta_{AAM} = 2^o$, $\beta = 1$, $\theta_t = 0$, $f_D^t = 0$, $\mathbf{w}$ is given by expression (2.63) and $\mathbf{c}^f(\theta_c^i, \theta_{AAM})$ by (2.16). In Fig. 7d the eigenvalues in dBs of the total disturbance covariance R are presented versus eigenvalue index for both the optimum and SMI schemes. Finally in Figs. 8a and 8b the average and maximum SINR error are plotted versus all 64 range bins of Fig. 5 where the average of average SINR error (AASE) of 7.2 dBs and average of maximum SINR error (AMSE) of 11.6 dBs succinctly characterize these figures.

In Fig. 9 the SMI-AASE is plotted as a function of the ratio of SMI samples, Lsmi, over the number of STAP degrees of freedom NM. From this figure it is noted that this ratio must be equal to 20 (corresponding to 5,120 SMI samples), to achieve an AASE value of 3 dB which is, at least, a factor of 10 larger than that required if the SAR

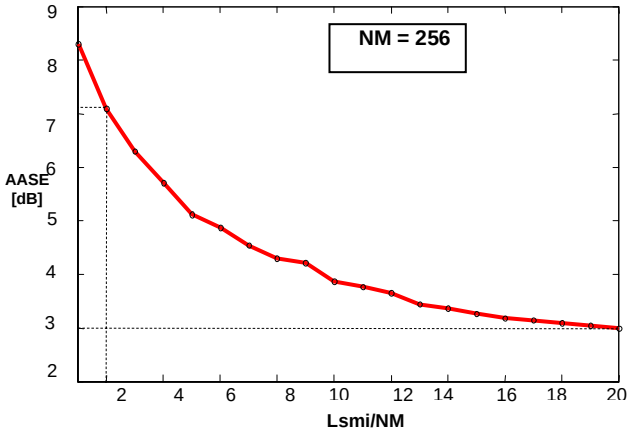

Fig. 9 SMI AASE Versus Lmsi/NM

image had been of a homogeneous terrain [2]. Clearly from this figure it is concluded that the derived SINR radar performance is not satisfactory for the SMI algorithm. These undesirable results have motivated researchers to look for better solutions using KA techniques [1]-[2]. In the next section two lossy source-coding techniques are offered that attempt to address the memory capacity problem associated with KA techniques.

3. RADAR BLIND & RADAR SEEING SOURCE CODERS

As mentioned earlier KA designs are motivated by the need to derive a superior SINR radar performance [1]-[2]. Unfortunately, however, to achieve this objective it is necessary that a high premium be paid in terms of memory storage and processing delay. In this section, two lossy source coding schemes are given that will attempt to address the memory storage requirements of KA-AMTI radar.

The rest of this section is organized as follows: First, a general description for an intelligent system is given using the front clutter covariance processor of a KA-AMTI radar as illustration; Second, a straightforward PT radar-blind SAR imagery compressor/decompressor is advanced that is highly appealing since it can be used with any radar system and outperforms the wavelets based JPEG2000 standard by more than 5 dBs [6]; Third and last, a PT radar-seeing SAR imagery compressor/decompressor is advanced that compresses the SAR imagery by a factor of 8,192 and also highly outperforms a JPEG2000 radar-seeing version.

3.1. Intelligent System Architecture

The general description for the intelligent system of Fig. 2 is given in Fig. 10. Its first salient feature is the intelligence section or signal source where the clutter is stored. The second part is the intelligence processor or signal processor. This processor uses the stored clutter, APRBG, and clutter steering vectors to compute the front clutter covariance matrix of (2.13). Although this system results in optimum SINR radar performance, it is highly inefficient in terms of both its memory storage and on-line computing hardware requirements. The intelligence processor for our KA-AMTI radar application is a straight clutter covariance processor defined from expression (2.13)-(2.14). The external input for these expressions is the front clutter source cell power ${}_f\sigma^2_{c,i}$ and its output is the front clutter covariance R_C^f .

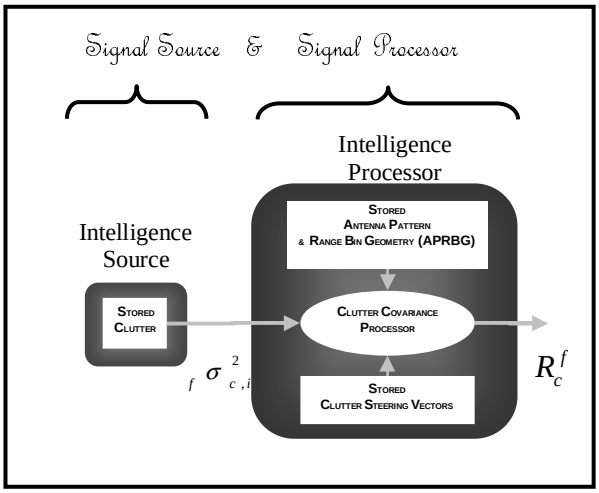

Fig. 10 Intelligent System

3.2. A Radar-Blind Intelligence Source Coder

In Fig. 11 the basic structure of a radar-blind (RB) intelligence source coder is depicted. It consists of a memory device containing the compressed clutter where the antenna pattern and range bin geometry was not used when designing the coder. The obvious advantage of a radar-blind scheme is that the compressed clutter can be used with any kind of airborne radar. A clutter decompressor is also necessary in order to derive an estimate for the clutter source cell power for use by the covariance processor.

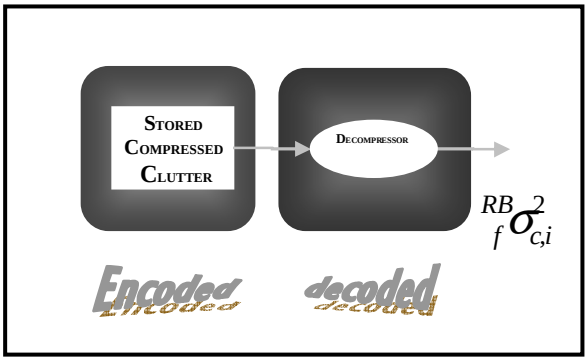

Fig. 11 Radar-Blind Intelligence Source Coder

Next in Fig. 12 a 512 bytes radar-blind PT decompressed SAR image is shown where the technical details of this PT compression technique are given in [6]. It is noted that the amount of compression is very significant, i.e., a factor of 8,192, since the original SAR image was compressed from 4 MB to 512 bytes. In [6] it is shown that this PT technique outperforms in signal to noise ratio (SNR) wavelets based JPEG2000 by more than 5 dBs. In Fig. 13 the corresponding average SINR error for all 64 range bins is presented (it

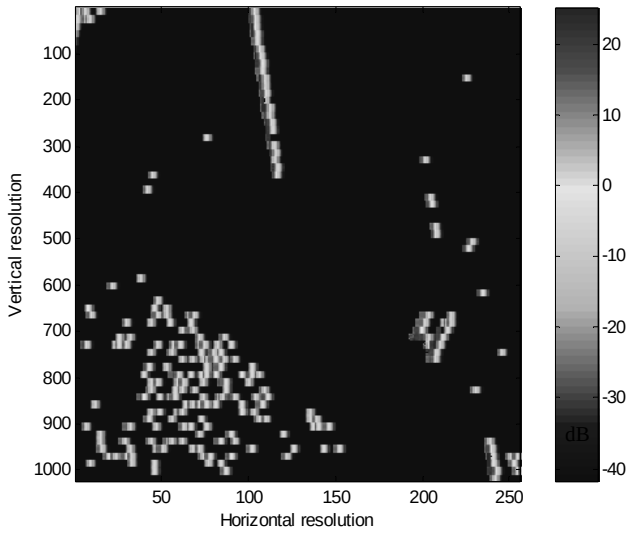

Fig. 12 512 Bytes Radar-Blind PT Decompressed SAR Image

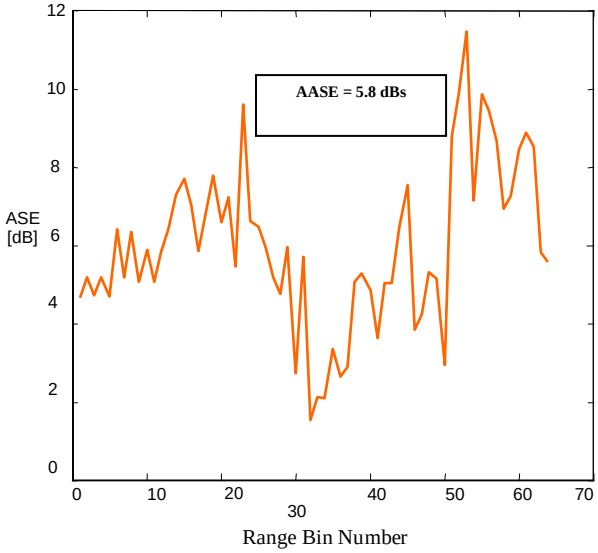

Fig. 13 Average SINR Error (ASE) versus Range Bin Number for Radar-Blind Case

should be noted that from Fig. 13 onwards all simulation results assume the radar parameter values given in Table 1 with the exception of the three jammers). An inspection of Figs. 13 reveals an AASE value of 5.8 dBs which is unsatisfactory for a KA type technique [1]-[2]. As mentioned earlier, in [7] this radar-blind technique is brought back to life when the covariance processor of expressions (2.13)-(2.14) are replaced with a new type of covariance processor, a type that is derived using a novel processor coding methodology, which is the time compression dual of space compression source coding. A radar-seeing technique is next considered that yields significantly better results than that derived with the radar-blind technique but that requires knowledge of the antenna pattern and range bin geometry or APRBG.

3.3. A Radar-Seeing Intelligence Source Coder

In Fig. 14 the basic structure of a radar-seeing (RS) intelligence source coder is presented where the coder has access to the APRBG. The scheme requires that minimum and maximum CNR values be found for our SAR image when processed in any direction; in the simulations 41 and 75 dBs were used for these values, respectively, which are also noted to be in accord with the CNR plot of Fig. 6. Using these extreme CNR values, the front clutter source cell power $_{f}\sigma^{2}_{c,i}$ was power limited to resides between 0.0077 and 7.7 which correspond to the minimum and maximum CNR values of 41 and 75 dBs, respectively, as well as the assumed front global antenna gain given in Table 1. The resultant power limited SAR image was then compressed using some standard compression scheme which in our case will be the PT source-coding scheme presented in [6]. In Fig. 15 a 512 bytes radar-seeing PT decompressed SAR image is shown for a compression ratio of 8,192. In Fig. 16 the corresponding average SINR error is given for the 64 range-bins of Fig. 5. Note that this figure is characterized by a very small AASE value of approximately 0.7 dBs. A comparison of Fig. 13 and Fig. 16 reveals that the radar-seeing scheme achieves much better SINR radar performance for the same amount of compression. However, it should be kept in mind, that this improvement is achieved at the expense of the prerequisite prior knowledge of the APRBG.

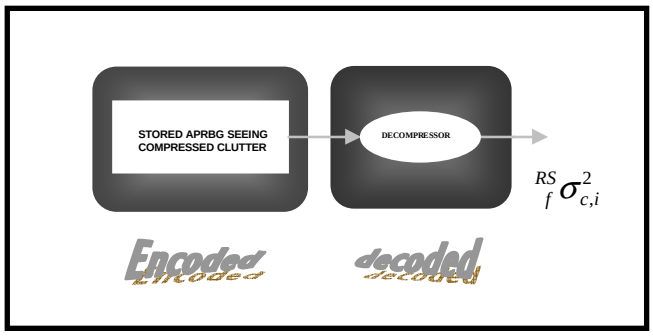

Fig. 14 Radar-Seeing Intelligence Source

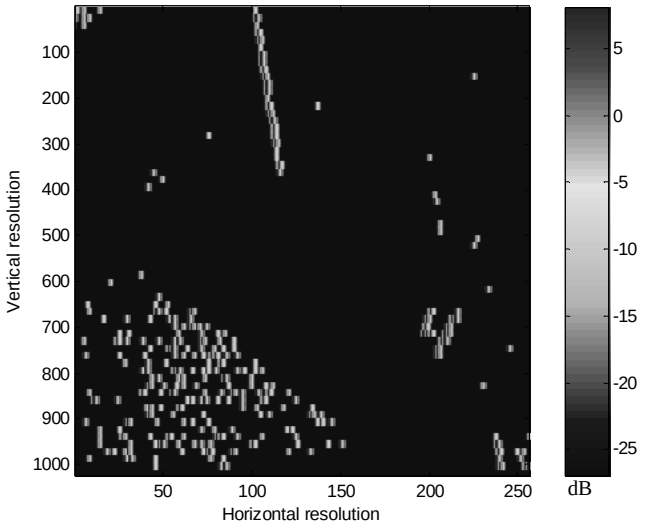

Fig. 15 512 Bytes Radar-Seeing PT Decompressed SAR Image

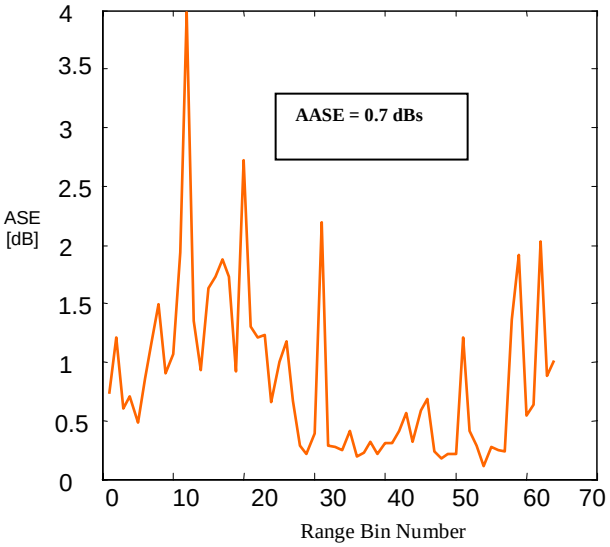

Fig. 16 Average SINR Error (ASE) versus Range Bin Number for Radar-Seeing Case

Table 1 Simulation Parameters

a.	Antenna	N = 16, M = 16, d/λ = ½, $f_r = 10^3$ Hz, $f_c = 10^9$ Hz, $K^f = 4x10^5$ or 56 dBs, $K^b = 10^{-4}$ or -40 dBs,
b.	Clutter	$N_c = 256$, β = 1, 41 dBs < $10\log_{10}CNR^f$ < 75 dBs, ${}_b\sigma^2_{c,i} = 1$ for all i, $10\log_{10}CNR^b$ = -40 dBs,
c.	Target	$\theta_t = 0^o$
d.	Antenna Disturbance	$\sigma_n^2 = 1$, $\theta_{AAM} = 2^o$
e.	Jammers	$N_J = 3$, $\theta_{J_1} = -60^o$, $\theta_{J_2} = -30^o$, $\theta_{J_3} = 45^o$, $10\log_{10}\sigma^2_{J_i}$ = 34 dBs for i=1,2,3, $10\log_{10}JNR_1$ = 53 dBs, $10\log_{10}JNR_2$ = -224 dBs and $10\log_{10}JNR_3$ = 66 dBs (**NOTE:** Jammers are only used in the **SMI** simulations of Figs. 7-9)
f.	Range Walk	ρ = 0.999999
g.	Internal Clutter Motion	b = 5.7, $\omega = 15$ mph
h.	Narrowband CM	ε_i =0 for all i, γ_i for all i fluctuates with a 5^o rms
i.	Finite Bandwidth CM	$\Delta\varepsilon = 0.001$, $\Delta\phi = 0.1^o$
j.	Angle Dependent CM	$B = 10^8$ Hz, $\Delta\theta = 28.6^o$
k.	Sample Matrix Inverse	Lsmi = 8x64=512, $\sigma^2_{diag} = 10$

4. CONCLUSIONS

In this paper it has been found that 2-D SAR imagery profiles can be highly compressed using radar-seeing compression techniques which can then be used in KA-AMTI radar systems subjected to severely taxing environmental disturbances. Among the many problems that remain to be studied and some of which are treated in [7] is the investigation of 3-D effects. The compressed SAR image that has been tested in this paper consists only of 2-D profiles which can be quite aspect dependent. Clearly when encountering mountains or cliffs, shadows will be created from certain vantage points as well as bright scattering points from other directions. Since these effects are angle-dependent their knowledge can be used to improve KA-AMTI radar system performance. The extension of the present approach to this more advanced 3-D scenario must be pursued.

REFERENCES

1. Proceedings of DARPA Kassper, 2002-2005.
2. Guerci, J.R. and Baranoski, E, " Knowledge-Aided Adaptive Radar at DARPA", *IEEE Signal Processing Magazine*, vol. 23, no. 1, pp. 41-50, January 2006.
3. J. D. Gibson, Editor-in-Chief, The Communications Handbook, *IEEE Press*, 1997
4. Taubman, D. S. and Marcellin, M., *JPEG2000: Image Compression Fundamentals, Standards and Practice*, Kluwer Academic Publishers, MA, 2002
5. Feria, E. H., "Super Predictive-Transform Coding", *USA Patent*, 2004
6. Feria, E. H. and Licul, D., "A Bit Planes Predictive-Transform Source Coder Illustrated with SAR Imagery", *Proceedings of SPIE Defense and Security Symposium*, 17-21 April 2006
7. Feria, E.H., "Compression-Designs for Knowledge-Aided AMTI Radar Systems", *Proceedings of SPIE Defense and Security Symposium*, 17-21 April 2006.
8. Ward, J., Space-Time Adaptive Processing for Airborne Radar, MIT Technical Report 1015, *MIT Lincoln Laboratory*, December 1994.
9. Guerci, J.R., " Space-Time Adaptive Processing for Radar", *Artech House*, 2003.

ACKNOWLEDGEMENTS

Dr. Joseph R. Guerci, the Director of DARPA's Special Projects Office (SPO), and Dr. Edward Baranoski, the Program Manager for DARPA's Knowledge-Aided Sensory Signal Processing Expert Reasoning (KASSPER), are gratefully acknowledged for their guidance during the course of this research. Their objective criticisms, advice and suggestions at every stage of this project are highly appreciated. Also my student Mr. Dalibor Licul's expert programming and computer networking skills greatly facilitated this research and for this I am indebted to him.